Supplementary information: Unified design of interaction and field-guided transport in active Janus colloid systems

Xuemao Zhou[1*], Liejie Lei[2*], Weiqi Liu[1], Fei Yang[1], Shuo Wang[3], Salah Eddine Ghellab[4]

[1]School of Physics and Information Engineering, Guangxi Science and Technology Normal University, 966 Tiebei Ave., Laibin, 546199, Guangxi, China.

[2]College of Aviation Engineering, Civil Aviation Flight University of China, 46 Nanchang road, Guanghan, 618307, Sichuan, China.

[3]Julong College, Shenzhen Technology University, 3002 Lantian Road, Shenzhen, 518118, Guangdong, China.

[4]Division of Chemistry and Biochemistry, Department of Chemistry and Chemical Engineering, Chalmers University of Technology, Kemigården 4, Gothenburg, 412 96, Västra Götaland, Sweden.

*Corresponding author(s). E-mail(s): zhouxuemao@gxstnu.edu.cn; leilijie@cafuc.edu.cn;

Keywords: Active colloids, Pair interaction, Light controlled motion, Swarming

Contents

Contents of supporting videos:

Video S1: Head on scattering from simulation.

Video S2: Head on scattering from experiment. Blue and green points denote the centers of particles 1 and 2, respectively; blue and green arrows indicate their velocity directions. White arrows represent particle orientations. Black points and arrows mark the center of mass of the interacting particle pair. The transient speeds of particle 1, particle 2, and the center of mass (labeled 3) are shown in each frame. The inset (where applicable) displays the motion in the center-of-mass frame.

Video S3: Parallel scattering from simulation.

Video S4: Parallel scattering from experiment. Blue and green points denote the centers of particles 1 and 2, respectively; blue and green arrows indicate their velocity directions. White arrows represent particle orientations. Black points and arrows mark the center of mass of the interacting particle pair. The transient speeds of particle 1, particle 2, and the center of mass (labeled 3) are shown in each frame. The inset (where applicable) displays the motion in the center-of-mass frame.

Video S5: Three colloids swarming. Particle motion is shown alongside the transient speed profile. The inset displays the motion in the frame of particle 2.

Video S6: Boundary guided motion. Red and blue points denote the centers of the active part and the full Janus particle, respectively. Red and black arrows indicate particle orientation and velocity, respectively. Dashed white lines mark the boundary of the dark band.

S1 Characterization of Janus colloids

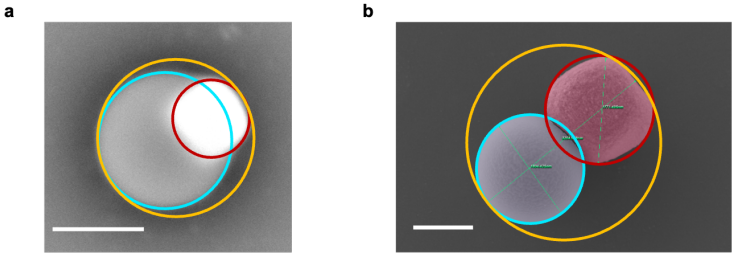

Fig. S1 SEM image of a standard (**a**) and dumbbell hematite/TPM (**b**) particle showing the definition of the size of TPM part r_p (blue circle), hematite part r_a (red circle) and the whole Janus particle r_J (orange circle). Scale bar = 1 µm.

The morphology of the Janus colloids was characterized using SEM. Follow previous definition [1], the size of TPM part r_p, hematite part r_a and the whole Janus particle r_J were measured as shown in Fig. S1. Thus, $d_\mathrm{c} = 2r_\mathrm{J} - r_\mathrm{a} - r_\mathrm{p}$ can be determined for each Janus particles. The statistics of d_c for different type of particles were shown in Table S1.

In the framework of ionic-diffusiophoresis, particle velocity is determined by $\mathbf{v} = \frac{\varepsilon}{4\pi\eta}\left(\frac{k_\mathrm{B}T}{Ze}\right)^2\left[\beta\bar{\zeta}(1-3\lambda) + \frac{1}{8}\bar{\zeta}^2\left(1-\frac{21}{2}\lambda\right)\right]\frac{\nabla c}{c}$, where ε and η are the permittivity and viscosity of the solution, $\beta = (D_+ - D_-)/(D_+ + D_-)$, D_+ and D_- are the diffusion coefficient of the cations and anions, $\bar{\zeta} = \frac{Ze\zeta}{k_\mathrm{B}T}$ is the normalized ζ potential, k_B is Boltzmann's constant, T is the temperature, Z is the number of charge e carried by a single ion, $\lambda = 1/\kappa a$ is the Debye length $\kappa^{-1} = (\frac{e^2}{\varepsilon k_\mathrm{B}T}\sum Z^2 c)^{1/2}$ normalized by the radius of the particle a, c is the generated concentration field [2]. When Janus colloids close to each other, the concentration field depends not only on the reaction of each particle, but also on the configuration/arrangement of particles, which varies with time. Therefore, when experimentally characterizing the mobility contrast $\mu_\mathrm{a}/\mu_\mathrm{p}$ of the Janus colloids during interaction, we neglect the concentration difference between the passive and active face for simplicity and in line with the essence of our theoretical model presented in Fig. 1a:

$$\frac{\mu_\mathrm{a}}{\mu_\mathrm{p}} = \frac{\beta\zeta_\mathrm{a}\frac{k_\mathrm{B}T}{Ze}(1-3\lambda) + \frac{1}{8}\zeta_\mathrm{a}^2(1-\frac{21}{2}\lambda)}{\beta\zeta_\mathrm{p}\frac{k_\mathrm{B}T}{Ze}(1-3\lambda) + \frac{1}{8}\zeta_\mathrm{p}^2(1-\frac{21}{2}\lambda)} \tag{1}$$

The ζ-potential of hematite colloids in DI water $\zeta_a = -27 \pm 3$ mV was measured using a zetasizer (Brookhaven Instruments NanoBrook 90Plus PALS). The ζ-potential of the TPM part of different types of Janus colloid was determined by measuring the ζ-potential of the homogeneously nucleated TPM formed during the synthesis. Without dewetting, i.e., without adding HCl, $\zeta_\mathrm{p} = -43 \pm 1$ mV for the standard type. For dewetted and dumbbell particles, i.e., with HCl, $\zeta_\mathrm{p} = -13 \pm 1$ mV. Therefore, the corresponding $\mu_\mathrm{a}/\mu_\mathrm{p}$ were list in Table S1.

Table S1 Characterization of hematite/TPM Janus colloids.

Type	r_p (μm)	r_a (μm)	r_J (μm)	$d_\mathrm{c}/r_\mathrm{p}$	$\mu_\mathrm{a}/\mu_\mathrm{p}$
Standard	0.88 ± 0.01	0.62 ± 0.01	1.16 ± 0.01	0.93 ± 0.03	1.14 ± 0.04
Dewetted	0.87 ± 0.01	0.41 ± 0.01	1.16 ± 0.01	1.19 ± 0.10	1.49 ± 0.09
Dumbbell	0.82 ± 0.07	0.75 ± 0.13	1.39 ± 0.14	1.46 ± 0.12	1.49 ± 0.09

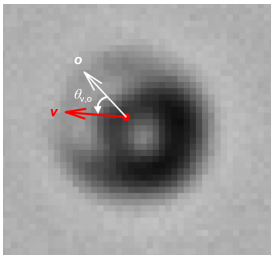

Fig. S2 Determination of particle location (red point), orientation ($\boldsymbol{o}$, white arrow), direction of velocity ($\boldsymbol{v}$, red arrow) and $\theta_{\mathrm{v,o}}$ in microscope images.

S2 Distinguishing between bounding and head-to-head dimer state

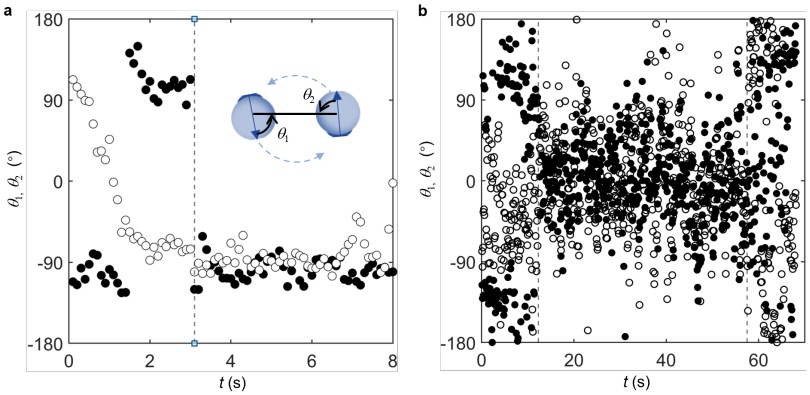

Fig. S3 The angle between particle orientation and the center-to-center line θ_1 and θ_2 during the circling bounding state (**a**) and the head-to-head dimer state (**b**). The vertical dashed lines indicate the period of bounding and dimer state.

The bounding state with particles circling around each other and the head-to-head dimer state with particles' passive face touching are well distinguished in athermal simulation. With thermal fluctuation in experiments, they appeared similar yet qualitatively different. Circling behavior exhibits non-zero angle between particle orientation and the center-to-center line θ_1 and θ_2 (Fig. S3a), and the angular velocity

ω maintains its direction (Fig. 2h). In contrast, for a head-to-head dimer, θ_1 and θ_2 fluctuated around zero (Fig. S3b), while ω alternate in sign (Fig. 1j).

S3 Three-particle swarming with varying mobility contrast and thermal intensity

Brownian dynamics simulations of three dancing Janus particles were performed with varying mobility contrast and thermal intensity. Initial configuration was presented in Fig. 3e. Particle 1 was assigned with parameters $\{d_c/r_p,\, \mu_a/\mu_p\} = \{1.2,\, 1.2\}$. Particle 2 and 3 were assigned with $d_c/r_p = 1.2$ and $\{\mu_a/\mu_p\} = 3, 4$ and 5. Simulations were performed with different thermal intensity, i.e., $D/D_0 = 0, 0.05, 0.25$ and 0.5. The resulting trajectories, MSD, probability distribution of $\theta_{v,o}$, autocorrelation function of particle orientation and velocity direction are summarized in Fig. S4 - S8, respectively.

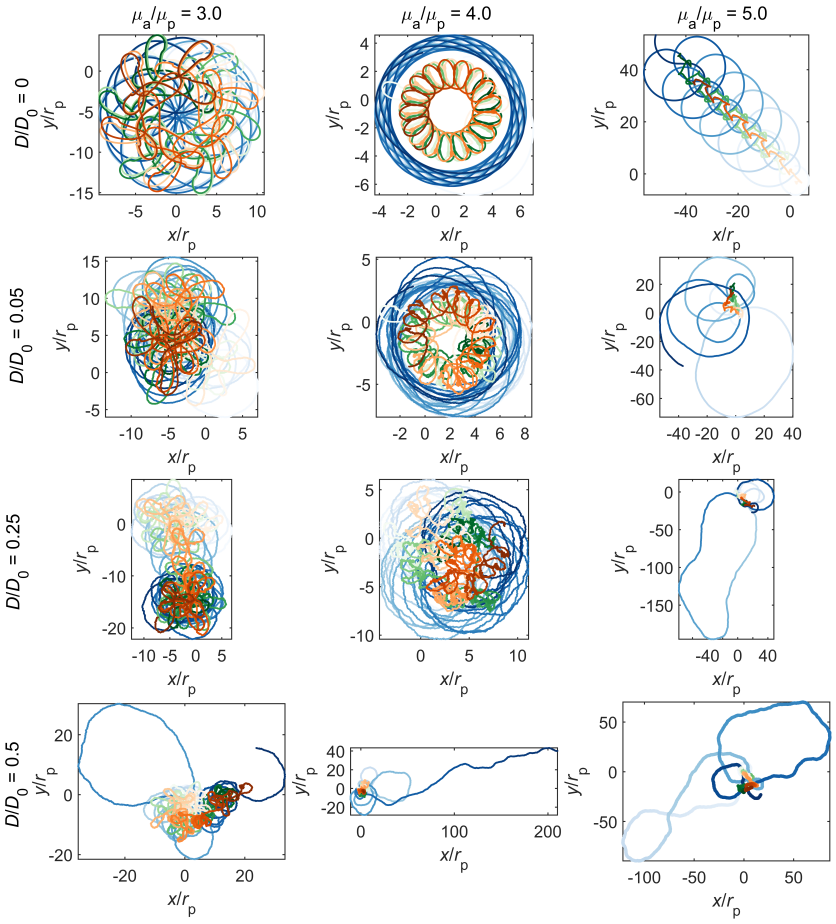

Fig. S4 Trajectories of three-particle swarming with varying mobility contrast and thermal intensity. Color coding is the same as in Fig. 3. Time progresses as color transitions from transparent to opaque.

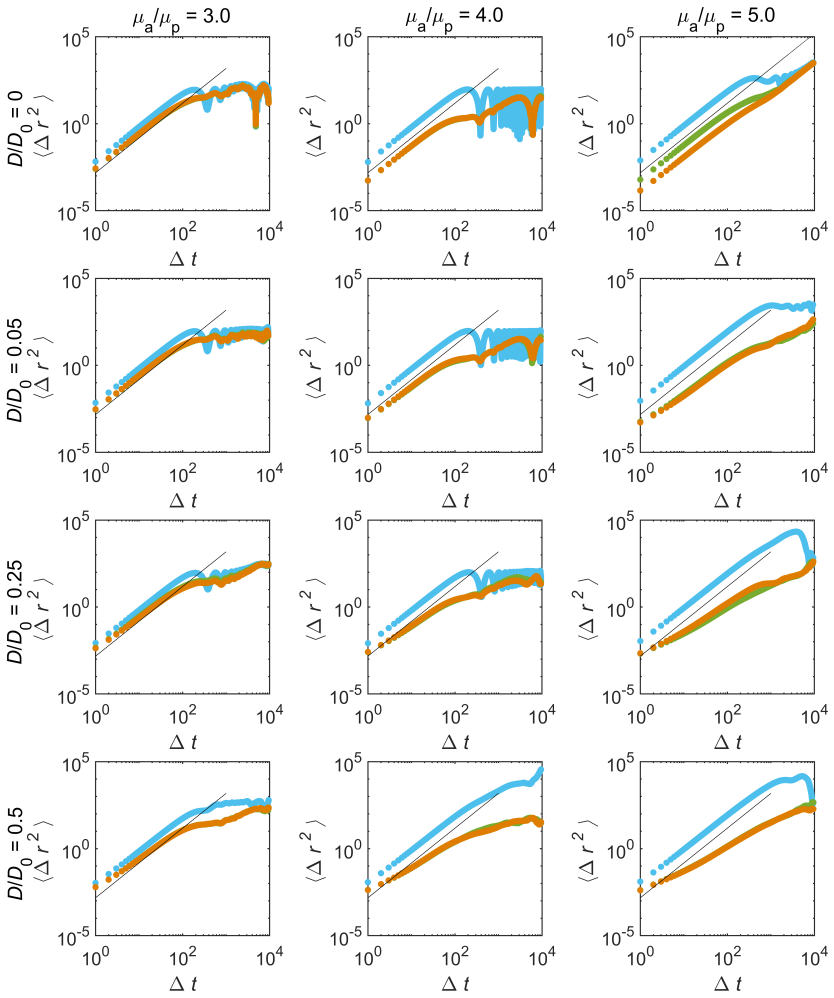

Fig. S5 MSD of three-particle swarming with varying mobility contrast and thermal intensity. Color coding is the same as in Fig. 3. Black lines indicate a slope of 2.

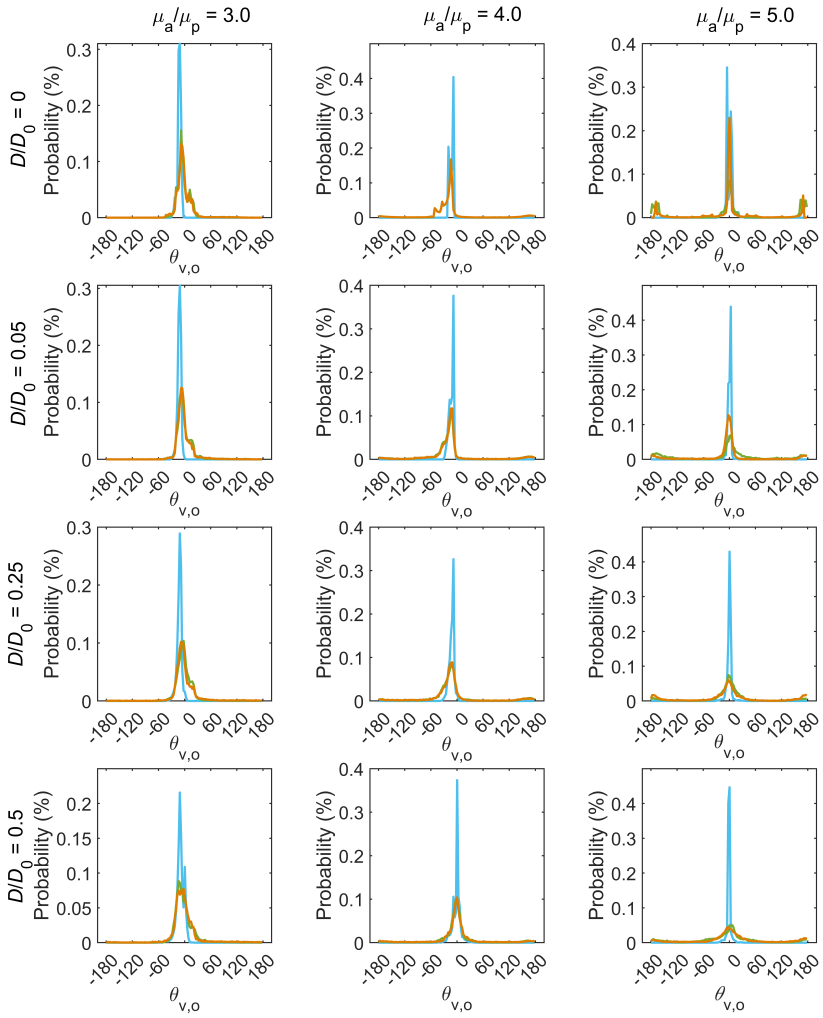

Fig. S6 Probability distribution function of $\theta_{v,o}$ of three-particle swarming with varying mobility contrast and thermal intensity. Color coding is the same as in Fig. 3.

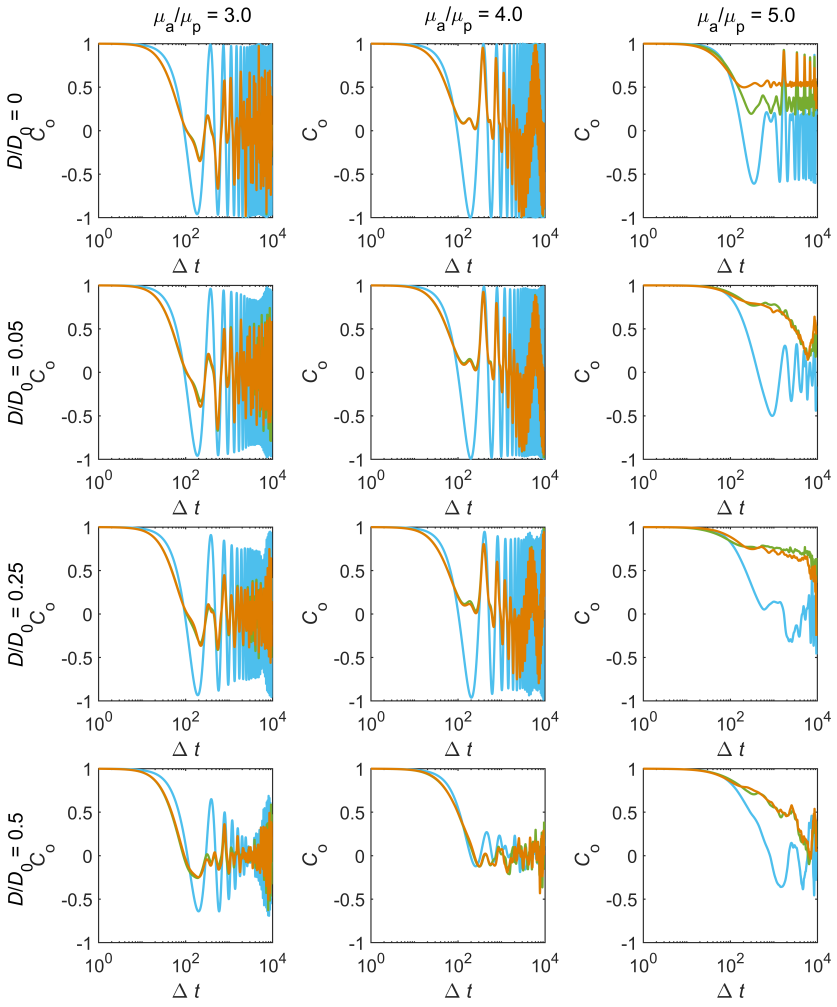

Fig. S7 Autocorrelation function of particle orientation of three-particle swarming with varying mobility contrast and thermal intensity. Color coding is the same as in Fig. 3.

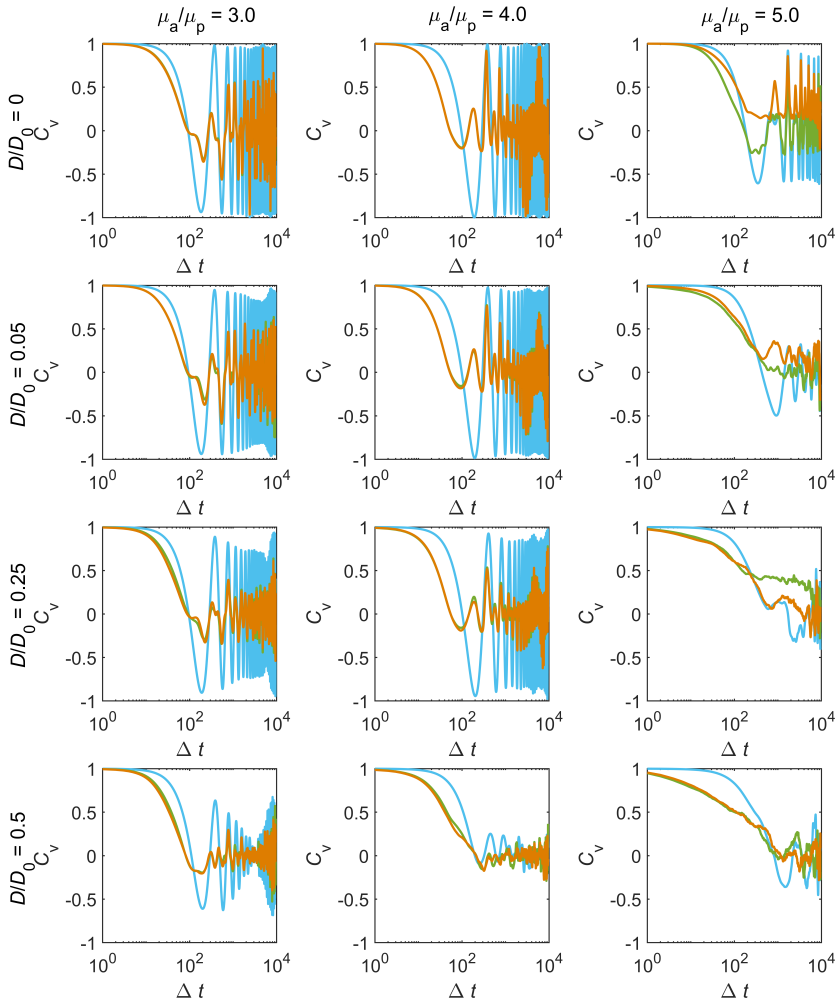

Fig. S8 Autocorrelation function of particle velocity direction of three-particle swarming with varying mobility contrast and thermal intensity. Color coding is the same as in Fig. 3.

S4 Average speed of dancing particles

Table S2 Estimating average speeds of dancing particles.

Particle	Average speed (μm s^{-1})		
	Transient speed	Short-time MSD	Full MSD
Particle 1	7 ± 5	10 ± 3	3.2 ± 0.1
Particle 2	6 ± 3	8 ± 2	3.3 ± 0.1
Particle 3	6 ± 3	7 ± 2	3.2 ± 0.2
Free particle	5 ± 2	7 ± 1	6.0 ± 0.1

There are three ways to estimate the average speed: averaged over transient speed, fitting to the short-time MSD and to the full MSD. Each of them provide different insights to the dynamics of an active colloid. Here, we discuss the average speed in the three-particle slingshot experiment.

The transient speed of 3 dancing particles and the free particle were presented in Fig. 4a. The averaged transient speed compares the mobility of particles, see main text and Table. S2. For the free particle, the standard deviation of the transient speed comes only from thermal fluctuation; while for the dancing particles, it also reflects the acceleration due to inter-particle interaction. The standard deviation of the transient speed of 3 dancing particles were greater than that of the free particle (2 μm/s); while that of the particle 1 was the largest (5 μm/s). It confirms that the particle 1 was the most susceptible to the inter-particle interaction, Fig. 4a and b. This is coincide with the C_o and C_v results that particle 1's autocorrelation functions decayed the fastest in short-time (< 1 s).

The MSD of the 4 particles were plotted in Fig. 3d. The full MSD follows [3, 4]:

$$\langle \Delta r^2 \rangle = 4D_0 \Delta t + \frac{V^2 \tau_\mathrm{R}^2}{3} \left(\frac{2\Delta t}{\tau_\mathrm{R}} + e^{-\frac{2\Delta t}{\tau_\mathrm{R}}} - 1 \right) , \tag{S2}$$

where D_0 is the free translational diffusion coefficient and τ_R is the characteristic time scale in rotational diffusion. At short-time, the MSD follows:

$$\langle \Delta r^2 \rangle = 4D_0 \Delta t + \frac{2}{3} V^2 \Delta t^2 \ , \ \Delta t \ll \tau_\mathrm{R}. \tag{S3}$$

The average speed estimated using short-time MSD excludes the thermal fluctuation leaving only the ballistic speed intrinsic to the particle [5]. For the dancing particles, speed from short-time MSD also includes the instantaneous acceleration due to the slingshot effect. By fitting the short-time MSD to Eq. S3 (Fig. S9a), average speed of particles were summarized in Table. S2. Particle 1 had the highest average speed and largest standard deviation, which agrees with the estimation based on transient speed.

The average speed obtained from full MSD characterize the ability of the active particle translating across the space in the long run. For the dancing particles, it reflects the mobility of the cluster as a whole. By fitting the full MSD to Eq. S2, average speed of particles were summarized in Table. S2. The full-MSD speed of 3 dancing particles were the same and their MSD overlapped at long time-scale (Fig. 4d and Fig. S9b). It clearly confirms that 3 particles moved as a cluster.

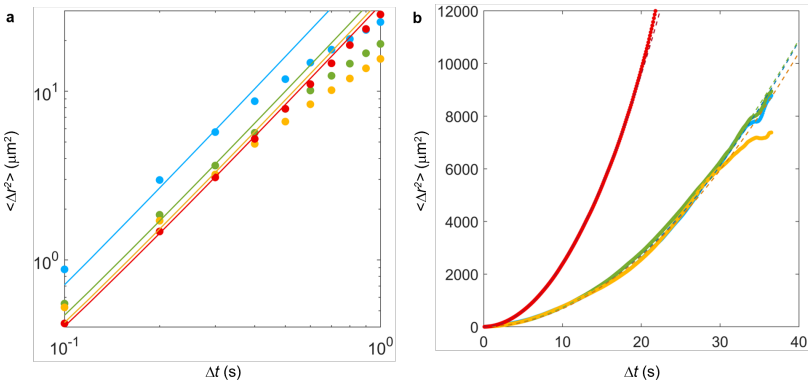

Fig. S9 Average speed of particles in 3 particle dancing experiments. The MSD results were replotted from Fig. 3d. Short (**a**) and full (**b**) time MSD were fitted to Eq. S3 and Eq. S2, respectively. Color code is the same as in Fig. 3, i.e., particle 1 (blue), 2 (orange), 3 (green) and free particle (red).

S5 Geometric invariance of trajectories under scaling c_0/α

We first examine the scenario where the initial orientation is tilted away from the upper boundary (left panel of Fig. S10). Interestingly, when we compare trajectories with different combinations of c_0 and α but identical ratios c_0/α, we observe a remarkable geometric invariance.

Specifically, the trajectories for $\{c_0, \alpha/\alpha_0\} = \{0.1, 0.5\}$ perfectly overlap with those for $\{0.2, 1\}$ in geometric shape (Fig. S11a). However, the particle with lower activity ($\alpha/\alpha_0 = 0.5$) traverses a shorter path within the same observation time compared to the particle with $\alpha/\alpha_0 = 1$, indicating a proportionally slower translational speed (Fig. S11b). Similarly, the trajectories for $\{0.1, 0.1\}$ and $\{0.5, 0.5\}$ exhibit identical geometric configurations, with the former progressing more slowly along the same spatial curve.

These observations suggest that the particle trajectories are geometrically invariant when the ratio c_0/α is held constant, differing only in the speed.

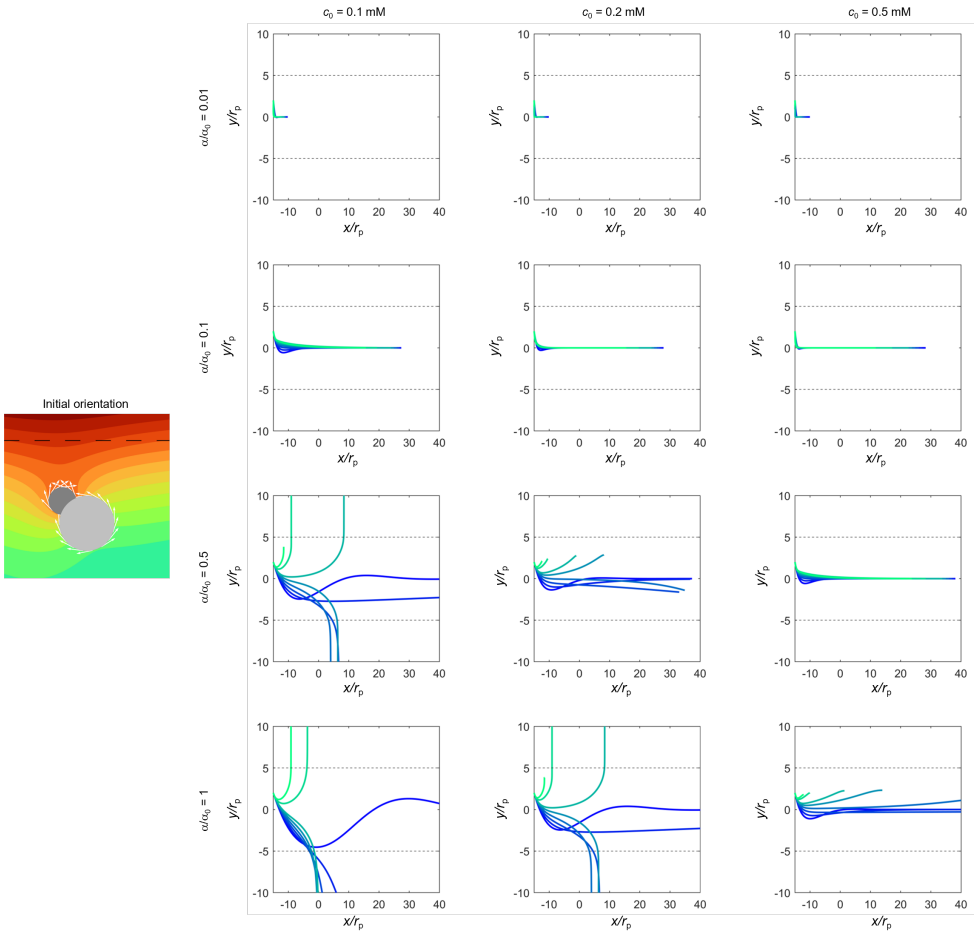

Fig. S10 Athermal trajectories of Janus particle in concentration bands with initial orientation tilted away from the upper boundary. From blue to cyan, $\mu_a/\mu_p = 0.5, 0.6, 0.7, 0.8, 0.9, 1.0, 1.5, 2.0$. All trajectories have the same time span.

S5.1 Scaling analysis

This geometric invariance can be understood through the scaling properties of the governing equations. In the athermal limit, the particle motion is described by:

$$\frac{\mathrm{d}\mathbf{r}}{\mathrm{d}t} = \mathbf{v}(\mathbf{r}), \tag{S4}$$

where the translational velocity is given by (Methods):

$$\mathbf{v}(\mathbf{r}) = -\frac{1}{S}\oint \mu(\mathbf{r}_s)(\mathbf{I} - \mathbf{nn}) \cdot \nabla c(\mathbf{r}_s)\,\mathrm{d}s. \tag{S5}$$

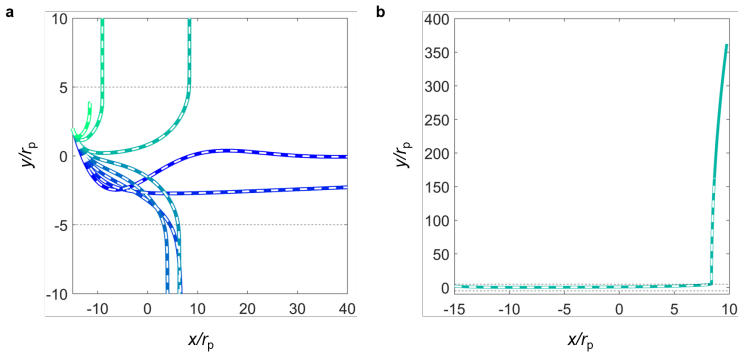

Fig. S11 Comparing trajectories of $\{c_0, \alpha/\alpha_0\} = \{0.2,\ 1\}$ (From blue to cyan, $\mu_a/\mu_p = 0.5, 0.6, 0.7, 0.8, 0.9, 1.0, 1.5, 2.0.$) with those of $\{0.1,\ 0.5\}$ (dashed white lines, corresponding μ_a/μ_p) at short timescale (**a**) and long timescale (**b**). All trajectories have the same time span.

Here, the total concentration field $c(\mathbf{r}_s) = c_{self}(\mathbf{r}_s) + c_{ext}(\mathbf{r}_s)$ comprises the self-generated field $c_{self} \propto \alpha$ (determined by surface activity) and the external field $c_{ext} \propto c_0$ (Methods).

When both α and c_0 are scaled by a factor k (i.e., $\alpha' = k\alpha$ and $c_0' = kc_0$), the total concentration field scales linearly as $c' = kc$. Consequently, the velocity field transforms as $\mathbf{v}'(\mathbf{r}) = k\mathbf{v}(\mathbf{r})$, and the governing equation becomes:

$$\frac{\mathrm{d}\mathbf{r}}{\mathrm{d}t} = k\mathbf{v}(\mathbf{r}). \tag{S6}$$

To preserve the geometric trajectory, we rescale time as $\tau = kt$, such that $\mathrm{d}t = \mathrm{d}\tau/k$. Substituting into Eq. S6 yields:

$$\frac{\mathrm{d}\mathbf{r}}{\mathrm{d}\tau} = \frac{\mathrm{d}\mathbf{r}}{\mathrm{d}t}\frac{\mathrm{d}t}{\mathrm{d}\tau} = k\mathbf{v}(\mathbf{r}) \cdot \frac{1}{k} = \mathbf{v}(\mathbf{r}). \tag{S7}$$

Since the trajectory is the integral curve of the differential equation, Eq. S7 demonstrates that the new particle with scaled parameters follows exactly the same geometric path as the original particle, but requires time $t' = t/k$ to reach the same position. This confirms the geometric invariance observed in simulations.

S5.2 Curvature scaling

The shape of the trajectory is characterized by its curvature κ, defined as the rate of change of the tangent angle ϑ with respect to arc length s:

$$\kappa = \frac{\mathrm{d}\vartheta}{\mathrm{d}s}. \tag{S8}$$

Recognizing that the angular velocity $\omega = \mathrm{d}\vartheta/\mathrm{d}t$ and the translational speed $v = \mathrm{d}s/\mathrm{d}t$, we obtain the fundamental relation:

$$\kappa = \frac{\omega}{v}. \tag{S9}$$

The angular velocity arises from the torque induced by the external field gradient. From the expression (Methods):

$$\boldsymbol{\omega} = -\frac{1}{A}\oint \mathbf{r} \times [\mu(\mathbf{r}_\mathrm{s})(\mathbf{I} - \mathbf{nn}) \cdot \nabla c(\mathbf{r}_\mathrm{s})]\,\mathrm{d}s, \tag{S10}$$

we see that $\boldsymbol{\omega}$ depends on the cross product of the position vector $\mathbf{r}$ (lever arm $\sim d_\mathrm{c}$) and the tangential force density (proportional to $\mu\nabla c_\mathrm{ext}$). Since $\nabla c_\mathrm{ext} \propto c_0/\delta$ (Methods), the magnitude scales as:

$$\omega \propto d_\mathrm{c}(\mu_\mathrm{a} - \mu_\mathrm{p})|\nabla c_\mathrm{ext}| \propto c_0. \tag{S11}$$

Conversely, acorrding to Eq. S5, the translational speed is dominated by the self-generated field when the external gradient is moderate, giving $v \propto \langle \bar{\mu} \cdot \nabla c_\mathrm{self} \rangle \propto \alpha$. Therefore, the curvature obeys the scaling law:

$$\kappa = \frac{\omega}{v} \propto \frac{c_0}{\alpha}. \tag{S12}$$

The ratio c_0/α determines the competition between external steering and self-propulsion:

Strong confinement ($c_0 \gg \alpha$, $\kappa \gg 1$): When the external field overwhelms self-propulsion, the particle experiences rapid reorientation toward the band center. The large curvature manifests as sharp turning near the boundary, followed by alignment along the x-axis (center of the band), consistent with the trajectories observed toward the top-right corner of Fig. S10.

Weak confinement ($c_0 \ll \alpha$, $\kappa \to 0$): When self-propulsion dominates, the trajectory becomes nearly ballistic with gentle curvature. Particles with low mobility contrast $\mu_\mathrm{a}/\mu_\mathrm{p}$ exhibit particularly weak steering, resulting in trajectories that gradually escape the band (lower left of Fig. S10), as the external field is insufficient to overcome the self-propulsion and reorient the particle toward the center.

S5.3 Effect of initial orientation

As trajectories are integral curves of the governing equations, they depend sensitively on initial conditions. Fig. S12 shows trajectories for particles initially oriented towards the upper boundary (left panel), demonstrating that despite the distinct path morphologies compared to Fig. S10, the geometric invariance and dynamical scaling with respect to c_0/α remain valid.

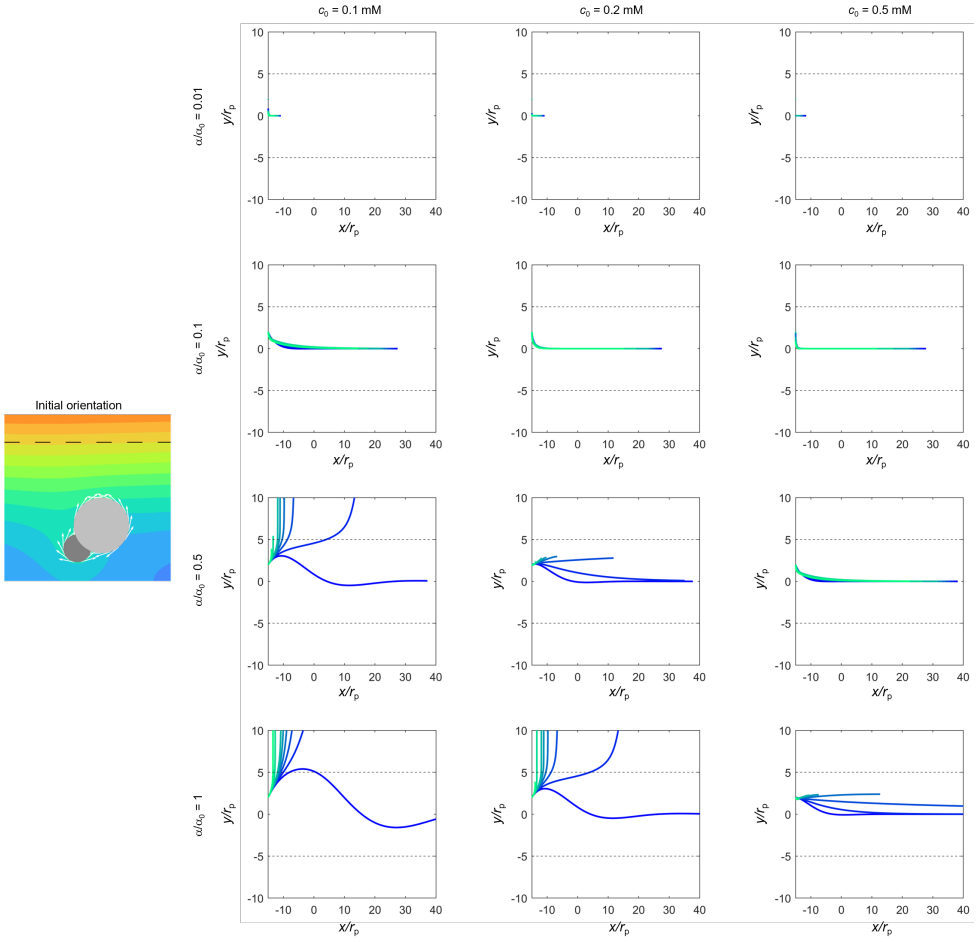

Fig. S12 Athermal trajectories of Janus particle in concentration bands with initial orientation tilted towards the upper boundary. From blue to cyan, $\mu_a/\mu_p = 0.5, 0.6, 0.7, 0.8, 0.9, 1.0, 1.5, 2.0$. All trajectories have the same time span.

S6 Light boundary guided motion

S6.1 The optical setup

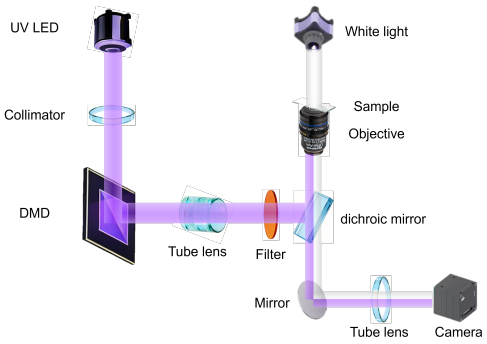

Fig. S13 Schematic of the DMD coupled microscope.

The optical system for generating light fields is schematically shown in Fig. S13. In the structured light path, illumination from a UV light-emitting diode (LED) is first collimated and subsequently deliver onto a digital micromirror device (DMD, DLP6500, Texas Instruments) to generate spatially patterned light. The modulated wavefront is then relayed via a tube lens (focal length: 180 mm) to the back focal plane of the 60 × oil objective (Olympus, NA = 1.4), which projects the patterned illumination onto the sample plane.

We used the transmitting light path of the invert microscope (Mingmei MF53) to observe particle dynamics. The white light provides the background illumination so that the bright-field images can be collected by the same objective and delivered to a camera (Ximea MQ042MG-CM) through a tube lens (focal length: 180 mm).

S6.2 Structured light

The light pattern reflected by the glass substrate is shown in Fig. S14a. The brightness and gradient are shown in Fig. S14b. The width of the dark band is defined as the distance between adjacent maximum and minimum of the gradient, as indicated by red dashed lines in Fig. S14b and Fig. 5e. Six dark bands between lighted area have the same width of 8.24 μm.

S6.3 Characterization of particle dynamics in the structured light

Fig. S15 presents the raw data used to construct the probability diagram in Fig. 5i. The dimer model predicts that particles orient perpendicular to the boundary, regardless of gradient strength. We therefore analyzed the orientation of dumbbell particles at both 0.66 mW/cm^2 and 1.09 mW/cm^2. The distance from the band center

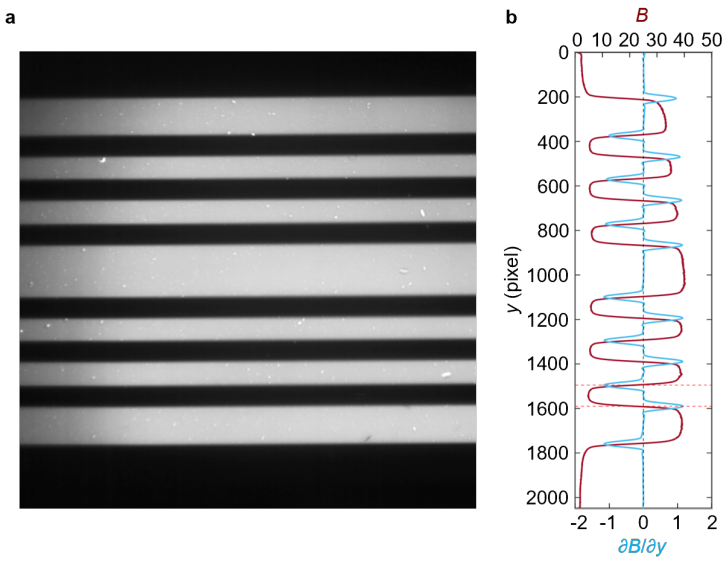

Fig. S14 **a**, Image of the structured light pattern. **b**, Brightness profile (B, red) and its gradient ($\partial B/\partial y$, blue). Red dashed lines indicates the boundary of a dark band. Black dashed line marks gradient equals 0.

(y coordinate) was discretized into bins of 0.5 μm width. $\bar{\theta}_{\mathrm{o}}$ is the averaged θ_{o} within each bin, plotted as blue filled circles in Fig. S15 and Fig. 5i.

For comparison, we analyzed the Brownian motion of the dumbbell particle with structured light turned off, using the same method as above. The x, y and full MSD are plotted in Fig. S16a. All MSDs follow a slop of 1, indicating unconfined Brownian motion. Fig. S16b shows the orientation distribution of dumbbell particles in Brownian motion, with no correlation between particle orientation and location. Notably, particles under structured light behave distinctly differently from those in Brownian motion.

The probability distribution of $\theta_{\mathrm{v,o}}$ for dumbbell particles within the dark band is plotted in Fig. S17a. In contrast to freely self-propelling Janus particles, which exhibit a narrow distribution of $\theta_{\mathrm{v,o}}$ centered around 0 (Fig. 1e), particles within the dark band show a broad distribution peaked at approximately 25°. For comparison, the distribution of $\theta_{\mathrm{v,o}}$ under Brownian motion (without structured light) is shown in Fig. S17b, with no preferred angle between velocity and orientation. Analysis of $\theta_{\mathrm{v,o}}$ confirms that particles within the dark band exhibit active motion, strongly guided by the concentration gradient established by structured light.

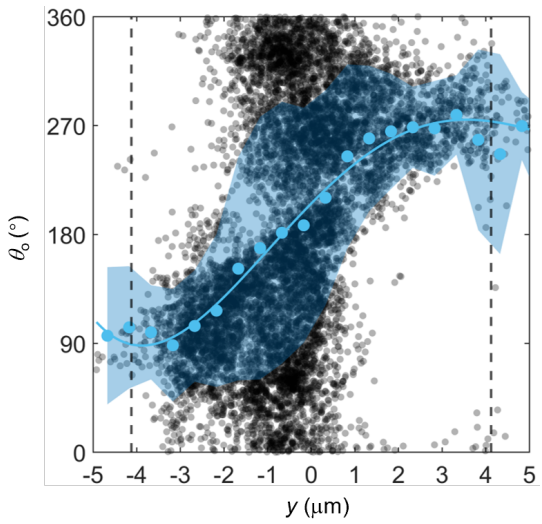

Fig. S15 Raw data of the colloidal orientation θ_o within the dark band (black filled circles). Blue filled circles: bin-averaged values; blue shaded region: corresponding standard deviation; blue curve: fourth-order polynomial fit. Black dashed lines denote the boundaries of the dark band.

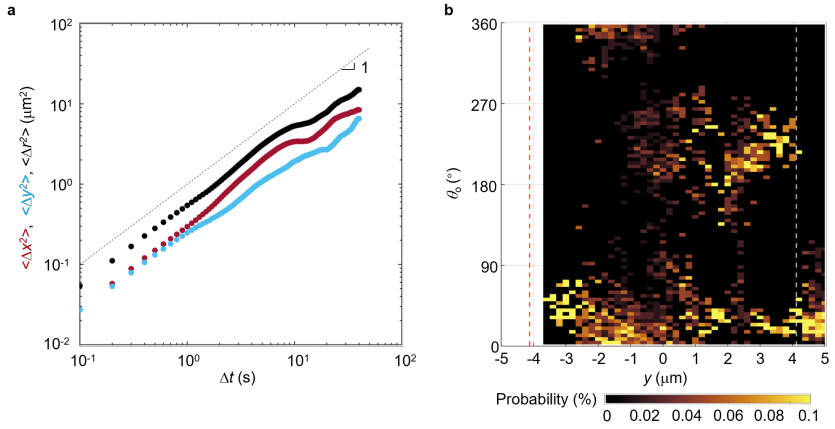

Fig. S16 The Brownian motion of dumbbell particles with structured light turned off. **a**, The x (red), y (blue) and full (black) MSD; dashed line indicates a slop of 1. **b**, Distribution of colloidal orientation θ_o.

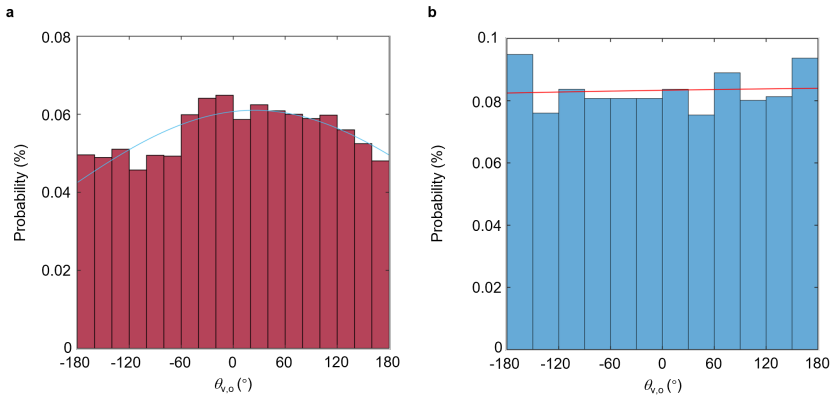

Fig. S17 The angle between velocity and orientation $\theta_{\mathrm{v,o}}$ for particles within the dark band (**a**) and without structured light (**b**). Curves represent Gaussian fits to the distributions.

References

[1] Lei, L., Cheng, R., Zhou, Y., Yang, T., Liang, B., Wang, S., Zhang, X., Lin, G., Zhou, X.: Estimating the velocity of chemically-driven Janus colloids considering the anisotropic concentration field. Frontiers in Chemistry **10**(August), 973961 (2022) https://doi.org/10.3389/fchem.2022.973961

[2] Zhou, X., Wang, S., Xian, L., Shah, Z.H., Li, Y., Lin, G., Gao, Y.: Ionic Effects in Ionic Diffusiophoresis in Chemically Driven Active Colloids. Physical Review Letters **127**(16), 168001 (2021) https://doi.org/10.1103/PhysRevLett.127.168001

[3] Howse, J.R., Jones, R.A.L.L., Ryan, A.J., Gough, T., Vafabakhsh, R., Golestanian, R.: Self-Motile Colloidal Particles: From Directed Propulsion to Random Walk. Physical Review Letters **99**(4), 8–11 (2007) https://doi.org/10.1103/PhysRevLett.99.048102

[4] Palacci, J., Cottin-Bizonne, C., Ybert, C., Bocquet, L.: Sedimentation and effective temperature of active colloidal suspensions. Physical Review Letters **105**(8), 1–4 (2010) https://doi.org/10.1103/PhysRevLett.105.088304

[5] Ebbens, S.J., Tu, M.H., Howse, J.R., Golestanian, R.: Size dependence of the propulsion velocity for catalytic Janus-sphere swimmers. Physical Review E - Statistical, Nonlinear, and Soft Matter Physics **85**(2), 1–4 (2012) https://doi.org/10.1103/PhysRevE.85.020401